

## Magnetically Soft and Hard Polypropylene/Cobalt Nanocomposites: Role of Maleic Anhydride Grafted Polypropylene

Qingliang He,<sup>†,‡</sup> Tingting Yuan,<sup>†</sup> Xi Zhang,<sup>†,‡</sup> Zhiping Luo,<sup>§</sup> Neel Haldolaarachchige,<sup>||</sup> Luyi Sun,<sup>⊥</sup> David P. Young,<sup>||</sup> Suying Wei,<sup>\*,‡</sup> and Zhanhu Guo<sup>\*,†</sup>

<sup>†</sup>Integrated Composites Laboratory (ICL), Dan F. Smith Department of Chemical Engineering, Lamar University, Beaumont, Texas 77710, United States

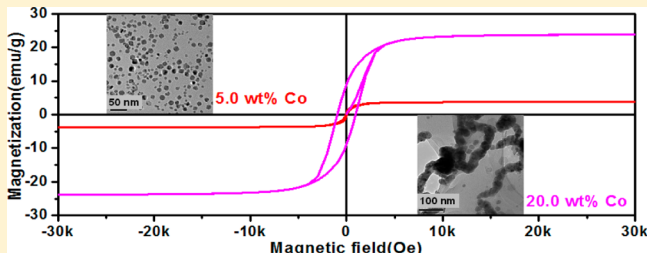
<sup>‡</sup>Department of Chemistry and Biochemistry, Lamar University, Beaumont, Texas 77710, United States

<sup>§</sup>Department of Chemistry and Physics and Southeastern North Carolina Regional Micro-analytical and Imaging Consortium, Fayetteville State University, Fayetteville, North Carolina 28301, United States

<sup>||</sup>Department of Physics and Astronomy, Louisiana State University, Baton Rouge, Louisiana 70803, United States

<sup>⊥</sup>Department of Chemistry and Biochemistry, Texas State University—San Marcos, San Marcos, Texas 78666, United States

**ABSTRACT:** Polypropylene (PP) magnetic polymer nanocomposites (MPNCs) filled with different loadings of cobalt (Co) nanoparticles (NPs) were synthesized through a one-pot bottom-up method, i.e., thermal decomposition of soluble dicobalt octacarbonyl ( $\text{Co}_2(\text{CO})_8$ ) in the refluxing xylene solution. Maleic anhydride grafted PP (PP-g-MA) served as surfactant to stabilize the in-situ formed Co NPs and control the particle morphology and served as compatibilizer to promote the particle dispersion in the hosting PP matrix. Transmission electron microscopy (TEM) micrographs revealed that the Co core NPs with a  $\text{Co}_3\text{O}_4$  shell were well distributed with an average size of 12.6 nm for 5.0 wt % Co loading, while an interconnected network structure was formed when the particle loading reached 10.0 wt %. X-ray diffraction (XRD) and X-ray photoelectron spectroscopy (XPS) results indicated that a thin  $\text{Co}_3\text{O}_4$  layer was formed on the surface of Co NPs together with chemisorbed hydrolyzed PP-g-MA. Differential scanning calorimetry (DSC) analysis demonstrated that the fusion heat and the crystalline fraction of the PP matrix decreased with the introduction of these NPs. Except the PP/5.0 wt % NPs sample, the observed monotonically decreased complex viscosity indicated a strong shear thinning behavior in the MPNC melts; meanwhile, the percolation took place at the particle loading between 5.0 and 10.0 wt %. The damping property suggested a strong interaction between the Co NPs and the hosting PP/PP-g-MA matrix. Thermal gravimetric analysis (TGA) and microscale combustion calorimetry (MCC) revealed an enhanced thermal stability and reduced flammability in the MPNCs. A magnetically soft behavior (coercivity of 47.0 Oe) was observed for the MPNCs at 5.0 wt % particle loading, while a magnetically hard behavior (coercivity of ~900–1000 Oe) was observed for the MPNCs at a loading of 10.0 wt % at room temperature.



### 1. INTRODUCTION

Magnetic polymer nanocomposites (MPNCs) have been extensively studied<sup>1–15</sup> due to their wide technological applications including electromagnetic interference (EMI) shielding,<sup>16</sup> high density information storage,<sup>17</sup> magnetic resonance imaging,<sup>18</sup> bimodal imaging agent,<sup>19</sup> wastewater purification,<sup>20</sup> and drug delivery.<sup>21</sup> Their magnetic properties have been considered to be strongly associated with the particle morphology (size and shape) and crystalline structure.<sup>13</sup> Among the transition metal iron group including Fe, Co, and Ni, Co has fairly large magnetization,<sup>22,23</sup> and its nanoparticles (NPs) have demonstrated size-dependent structural, magnetic, electronic, and catalytic properties.<sup>24</sup> The reported chemical approaches to prepare Co NPs include the decomposition of organo-metal precursors,<sup>25–39</sup> cobalt salt reduction,<sup>40</sup> and solvothermal reaction using cobalt salt<sup>41</sup> in organic solvents in the presence of different surfactants/polymers as dispersant

or stabilizer. The conventionally used small molecular weight surfactants such as oleic acid,<sup>32,35–37,39</sup> trioctylphosphine (TOP),<sup>40</sup> and TOP oxide (TOPO)<sup>28</sup> are vital to prepare well-dispersed magnetic NPs due to the intrinsic dipole–dipole interactions and high surface energy of the NPs.

Polymers possessing functional groups in their backbones or polar structures including poly(methyl methacrylate),<sup>4</sup> poly(styrene-*b*-4-vinylphenoxyphthalonitrile),<sup>22</sup> poly(sodium 4-styrenesulfonate),<sup>23</sup> poly(acrylic acid)-*b*-polystyrene,<sup>40</sup> polystyrene-*b*-poly(4-(phenylethynyl)styrene,<sup>42</sup> and poly(vinylpyrrolidone)<sup>43</sup> have been reported to serve as the hosting polymer matrices for magnetic Co NPs, in which the Co NPs are stable and dispersed fairly well. On the other hand,

Received: January 20, 2013

Revised: March 1, 2013

Published: March 15, 2013

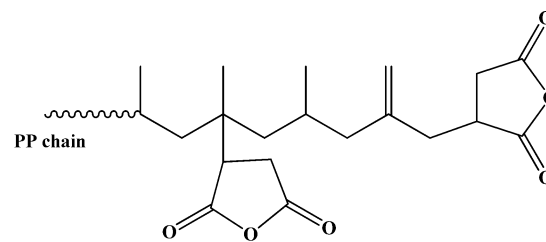
nonpolar inert polymers such as polyolefin are nonideal to host the Co NPs. Commodity plastic polyolefins, produced from simple hydrocarbon olefin monomers, have been deployed with about 53 million tons in 2010<sup>44</sup> for a wide range of areas including packaging,<sup>45</sup> containers,<sup>46</sup> automotives,<sup>47,48</sup> and industrial parts<sup>49–53</sup> due to their low energy consumption for processing, high chemical resistance, and good processability.<sup>54,55</sup> Polypropylene (PP), one of the most widely used commodity plastics,<sup>56,57</sup> has poor performance in the nanocomposites with many kinds of nanofillers due to the lack of reactive sites in the inert PP backbone causing the weak interfacial interactions between PP matrix and nanofillers. Poor dispersion is another drawback to obtain nanocomposites with desired performance due to the high surface energy and large specific surface area of the nanofillers. Therefore, surfactants and stabilizers are normally used to overcome these drawbacks and to enhance the performances of these nanocomposites. However, small molecule surfactants like oleic acid are only for the synthesis of stabilized magnetic nanostructure assembly rather than for preparing PP MPNCs. Conventional plastic additive—maleic anhydride (MAH) grafted PP (named PP-g-MA) has potential to be an alternative surfactant to prepare PP MPNCs due to its similar backbone structure as PP and polar MAH groups, which can effectively enhance the interfacial interactions by creating entanglements on both sides of the interfaces between the polymer matrix and the fillers.<sup>58,59</sup> PP-g-MA has been reported to serve as coupling agent/compatibilizer between the polymer matrix and different fillers like organoclay,<sup>60,61</sup> double-layered hydroxides,<sup>62</sup> and carbon nanotubes.<sup>63,64</sup> However, the suitability of PP-g-MA in stabilizing magnetic Co NPs is still unclear. In addition, as a flammable polymer, metal hydroxides,<sup>65,66</sup> phosphorus-containing compounds,<sup>67</sup> and intumescent flame retardants<sup>68,69</sup> are commonly used to effectively reduce the flammability of PP. However, the thermal stability and flame retardancy of sole metal Co NPs on the PP matrix have been rarely reported.

In this work, stabilized PP MPNCs filled with Co NPs have been successfully prepared through a facile in-situ thermal decomposition of  $\text{Co}_2(\text{CO})_8$  in the refluxing PP/xylene solution in the presence of PP-g-MA as stabilizer. The MPNCs with a nanoparticle loading of 5.0, 10.0, 15.0, and 20.0 wt % were prepared. The crystalline structure and morphology of the NPs were investigated by X-ray diffraction (XRD) and transmission electron microscopy (TEM). The interfacial interactions between the NPs and the PP/PP-g-MA matrix were studied by X-ray photoelectron spectroscopy (XPS). The thermal property was investigated by thermogravimetric analysis (TGA) and differential scanning calorimetry (DSC), and the flammability/flame retardancy was assessed by microscale combustion calorimetry (MCC). The melt rheological behaviors and magnetic properties were also investigated. Both the shape anisotropy and the interparticle interaction have been used to interpret the observed magnetic property differences in the MPNCs with different loadings.

## 2. EXPERIMENTAL SECTION

**2.1. Materials.** The PP used in this study was supplied by Total Petrochemicals USA, Inc. ( $\rho = 0.9 \text{ g/cm}^3$ ,  $M_n \approx 40\,500$ ,  $M_w \approx 155\,000$ , melt index  $\approx 35 \text{ g/min}$ ). PP-g-MA (with  $M_n \approx 8000$ ,  $\rho = 0.90 \text{ g/cm}^3$ , provided by Baker Hughes Inc.) used was a homopolypropylene with one terminal MAH through Alder-ENE reaction and an additional MAH grafting (the chemical structure is shown in Scheme 1). Dicobalt octacarbonyl ( $\text{Co}_2(\text{CO})_8$ , stabilized with 1–5% hexane)

**Scheme 1. Chemical Structure of PP-g-MA**



was purchased from Strem Chemicals Inc. Solvent xylene (laboratory grade,  $\rho = 0.87 \text{ g/cm}^3$ ) was purchased from Fisher Scientific. All the chemicals were used as-received without any further treatment.

**2.2. Synthesis of Polymer Nanocomposites.** The brief procedures for preparing the PP MPNCs are as follows. First, 9.0 g of PP pellets, 0.5 g of PP-g-MA, and 100 mL of xylene were added into a 500 mL three-neck round-bottom flask. The mixture was then heated to the boiling temperature of xylene (~140 °C) and refluxed for 2 h in order to dissolve PP and PP-g-MA. Meanwhile, 1.45 g of  $\text{Co}_2(\text{CO})_8$  was dissolved in 30 mL of xylene in a glovebox under nitrogen protection. After the dissolution of polymers in xylene, the solution was cooled to around 120 °C, and then the prepared  $\text{Co}_2(\text{CO})_8$ /xylene solution was injected into the flask to obtain a 5.0 wt % Co-PP MPNCs (calculation was based on the pure cobalt element weight fraction). For 5.0, 10.0, 15.0, and 20.0 wt % Co loading, the PP pellets used were 9.0, 8.5, 8.0, and 7.5 g, while the PP-g-MA concentration in final MPNCs was fixed at 5.0 wt % for all the samples. The Co loadings in this study were controlled at 0.0, 5.0, 10.0, 15.0, and 20.0 wt % with a corresponding weight of 0.0, 1.45, 2.90, 4.35, and 5.80 g of  $\text{Co}_2(\text{CO})_8$ . The solution immediately turned from transparent to brown and then gradually black during the refluxing process for an additional 4 h. The reflux speed was controlled at ~1–2 drops/s to maintain a smooth reaction. Finally, the solution was cooled to room temperature in the flask and then poured into a large glass container to evaporate solvent in the fume hood overnight. The black powders were then dried in a vacuum oven at room temperature overnight. Pure PP and the PP/20.0 wt % Co MPNCs (8.0 g of PP and 5.8 g of  $\text{Co}_2(\text{CO})_8$  without PP-g-MA) were also prepared as references using the same procedures.

$\text{Co}_2(\text{CO})_8$  underwent a series of thermal decomposition reactions with releasing carbon monoxide under constant heating in organic solvent. The thermal decomposition of  $\text{Co}_2(\text{CO})_8$  was complex and normally went through intermediates such as  $\text{Co}_4(\text{CO})_{12}$  and  $\text{Co}_6(\text{CO})_{16}$  (black color) and other unstable mononuclear Co carbonyls.<sup>70</sup> After reaction at ~140 °C for several hours,  $\text{Co}_2(\text{CO})_8$  was fully decomposed accompanied by the formation of the metallic Co NPs from the growth of Co nuclei.<sup>70</sup> Meanwhile, a layer of Co oxide was formed on the surface of the Co NPs upon oxidization in air.

The desired samples were prepared from the final powders (with different Co loadings in the PP matrix) using hot press molding machine (model: Carver 3853-0). The concise procedures were as follows. First, the powders were added into a cylinder-shaped mold, which was placed between the two panels in the molding machine. Second, the mold was heated to 180 °C at a heating rate of 20 °C/min under a pressure of 10 MPa and then maintained at 180 °C for 5–10 min to ensure the formation of compact samples. Finally, the sample was cooled naturally to room temperature in the mold.

**2.3. Characterization.** X-ray diffraction (XRD) analysis was carried out with a Bruker AXS D8 Discover diffractometer operating with a Cu K $\alpha$  radiation source. The XRD patterns were recorded at  $2\theta$  from 30° to 60°.

A transmission electron microscope (TEM) was used to characterize the particle morphology of the as-prepared PP MPNCs in a FEI TECNAI G2 F20 microscope at a working voltage of 200 kV. The samples were prepared from the hot solution of the PP MPNCs at the end of synthesis process. One droplet of the diluted hot solution containing the NPs was dropped on a 400-mesh carbon-coated copper grid (Electron Microscopy Sciences).

Scanning electron microscopy (SEM) was further utilized to demonstrate the dispersion of the NPs in the PP matrix in the presence/absence of PP-g-MA. The samples were precipitated upon the colloidal samples and were dried into composite powders. The samples were mounted on an aluminum stub by using carbon tape. Then, the samples were sputtered in a Hummer 6.2 system (15 mA AC for 30 s), creating an ~1 nm thick film of Au. SEM used was a JEOL JSM 6700R in high-vacuum mode.

The interaction of the PP/PP-g-MA with the Co NPs was studied by X-ray photoelectron spectroscopy (XPS) on a Kratos AXIS 165 system. The scan of each sample was carried out with a monochromatic Al X-ray source at the anode of 10 kV and beam current of 15 mA.

The thermal stability of the pristine PP and its MPNCs was investigated using thermogravimetric analysis (TGA, TA Instruments Q-500). The samples were heated from room temperature to 700 °C at a constant heating rate of 20 °C/min under air and N<sub>2</sub> gas atmosphere, respectively. The flow rate was 60 mL/min under both two atmospheres.

Microscale combustion calorimetry (MCC) was utilized to determine/assess the flammability/fire hazards by measuring the heat release related parameters. To be specific, heat release capacity (HRC), rate of heat release (HRR) at different temperatures, peak rate of heat release (PHRR), temperature at PHRR ( $T_{PHRR}$ ), and total heat release (THR) can be obtained from MCC. Here, the data were recorded according to a standard method ASTM D7309-2007 (method A) using a "MCC-2" calorimeter produced by Govmark Inc. In a typical measurement, about 5 mg of the sample was heated from 80 to 650 °C using a heating rate of 1 °C/s in a continuous stream of nitrogen flowing at 80 mL/min. The thermal decomposition products (also named as "fuel gases") were mixed with a 20 mL/min stream of oxygen before entering a 900 °C combustion furnace to complete the nonflaming combustion.

Differential scanning calorimetry (DSC) was carried out on a TA Instruments Q2000 calorimeter with typical heat-cool-heat procedures. 5–10 mg of the sample was encapsulated in an aluminum pan, heated from 0 to 180 °C at a heating rate of 10 °C/min under a N<sub>2</sub> flow rate of ~50 mL/min, and then stayed at 180 °C for 1 min. After that, the specimen was cooled to room temperature at a rate of -10 °C/min and then heated from room temperature to 180 °C at the same heating rate. The data enclosed here were collected from the first cooling and the second heating procedures in order to remove the heat history of the specimens.

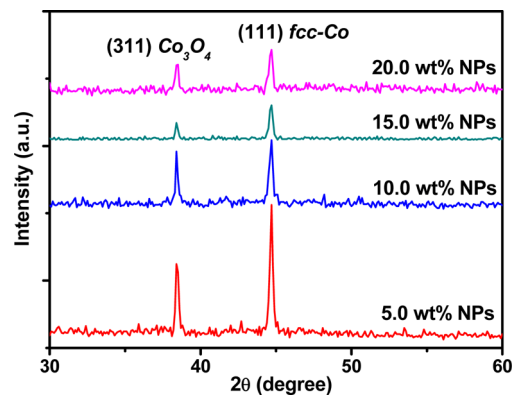
The rheological behaviors of the PP melts and its MPNC melts were studied using a TA Instruments rheometer (type AR 2000ex). Environmental test chamber (ETC) steel parallel-plate geometry (25 mm in diameter) was used to perform the measurements. A dynamic strain sweep at 1 rad/s was performed in order to determine the limit of linear viscoelasticity. Then, dynamic oscillation frequency was swept from 100 to 0.1 Hz in the linear viscoelastic range with a strain of 1.0% at 200 °C under air atmosphere. The sample used here was molded from the prepared composite powders through hot press to form a cylindrical shape with 25 mm in diameter and around 2 mm thickness.

The magnetic property measurements of all the PP MPNCs were carried out in a 9 T physical properties measurement system (PPMS) by Quantum Design at room temperature.

### 3. RESULTS AND DISCUSSION

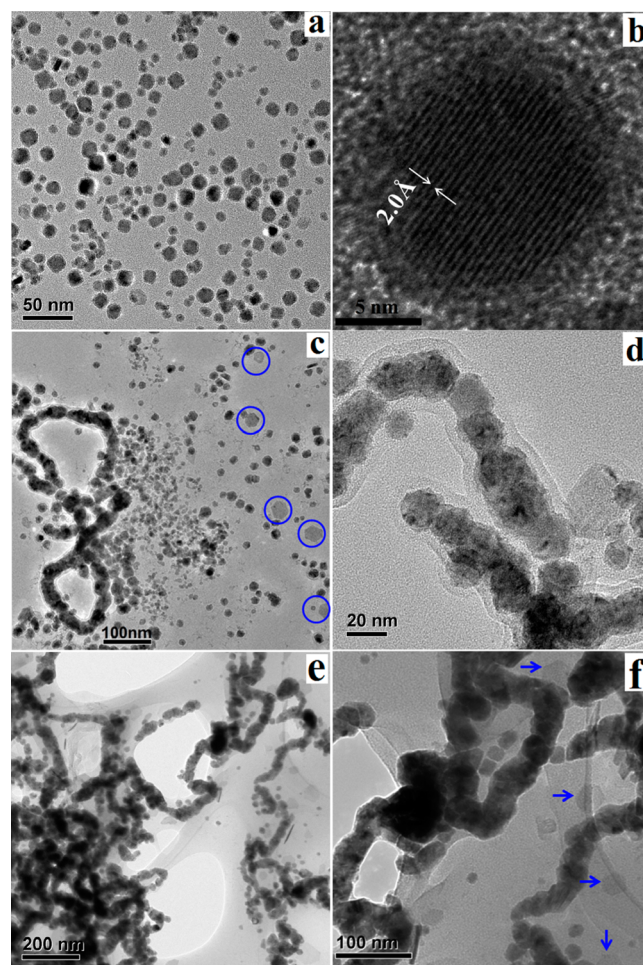
#### 3.1. Structural and Morphological Characterization.

Figure 1 shows the XRD patterns of the as-prepared PP MPNCs with different loadings. Two strong peaks are observed. The first one with  $2\theta$  of around 37° is assigned to (311) plane of Co<sub>3</sub>O<sub>4</sub> (PDF# 42-1467), and the second one with  $2\theta$  of around 44.7° can be assigned to either (002) plane of hexagonal closed packed (hcp)-metallic Co (PDF# 05-0727) or (111) plane of face centered cubic (fcc)-metallic Co (PDF# 15-0806). However, due to the absence of other two strong characteristic peaks at 41.7 and 47.6° of hcp-metallic Co, the



**Figure 1.** XRD patterns of PP/PP-g-MA/Co nanocomposites with different loadings of Co NPs.

Co formed here is determined as fcc-structure. The XRD results indicated that the in-situ formed Co NPs have a metallic core surrounded by a Co<sub>3</sub>O<sub>4</sub> shell, which can be further confirmed from TEM images. For PP MPNCs with 5.0 wt % Co NPs, TEM image demonstrated that these as-synthesized Co NPs were well dispersed in the PP matrix with an average size of 12.6 nm and an oxide shell of 1–2 nm thickness (Figure 2a). The observed wide particle size distribution is primarily attributed to the Ostwald ripening mechanism.<sup>22,23,36</sup> An



**Figure 2.** TEM images of PP/PP-g-MA/Co nanocomposites with 5.0 wt % (a, b), 10.0 wt % (c, d), and 20.0 wt % Co NPs (e, f).

observation of 2.0 Å lattice spacing from high-resolution TEM (HRTEM) (Figure 2b) further supported the fcc-Co (PDF# 15-0806) crystalline structures. In addition, typical NPs exhibited a dark core surrounded by a gray shell structure.

When the particle loading increased to 10.0 wt %, the in-situ synthesized Co NPs were partially assembled into nanowires and the rest were polydispersed (Figure 2c). A closer observation revealed that the curvy nanowires consisted of core–shell NP chains with an average diameter of ~22.4 nm (Figure 2d). It is worth noting that in addition to these Co nanowires and NPs several light-color hexagonal structural NPs were formed in the MPNCs (blue circle areas in Figure 2c). When the particle loading was further increased to 20.0 wt %, the majority of the Co NPs were assembled into nanowires with an average diameter of ~42.7 nm (Figure 2e). The light hexagonal structure NPs can also be observed (blue arrays in Figure 2f).

Although the TEM samples were made from the drop-casting method, the formed films for other tests were also processed from the same colloids in the same precipitated way. And thus the TEM images reflect the true particle distribution in the measured samples in a projected 2-D way. Furthermore, in order to confirm the particle dispersion quality, the real 2-D surface observation was also carried out by SEM on the dried samples. Specifically, in order to further identify the nanoscale dispersion and stabilization of the in-situ synthesized Co NPs in the PP matrix with the aids of PP-g-MA, a reference sample with only 20.0 wt % Co loading in the PP matrix (without PP-g-MA) was also synthesized for comparison. With the precipitated sample, the SEM image in Figure 3a clearly

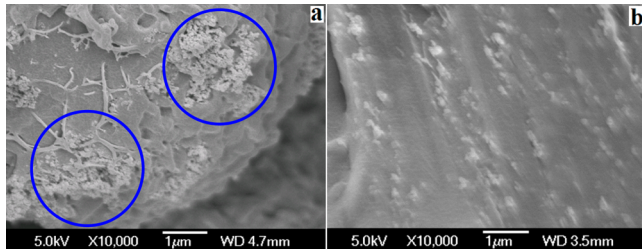


**Figure 3.** SEM images of (a) PP/20.0 wt % Co nanocomposites and (b) PP/20.0 wt % Co nanocomposites with 5.0 wt % PP-g-MA.

demonstrated the agglomerated Co NPs (in the blue circle area) exposed on the surface of the PP matrix with a poor dispersion quality when the PP matrix was directly filled with the 20.0 wt % Co NPs. These agglomerations took place due to the lack of the Co nanoparticle stabilization by any surfactant. Meanwhile, the well-defined chainlike Co nanostructures were clearly observed to be uniformly embedded in the PP matrix (Figure 3b) when 5.0 wt % PP-g-MA was utilized to stabilize the 20.0 wt % Co NPs. Thus, it is indisputable to claim that the nanoscale Co NPs can be effectively stabilized and dispersed in the PP matrix by a small amount of PP-g-MA.

**3.2. XPS Analysis.** XPS is powerful to characterize the surfaces of solid samples, i.e., to identify the atomic composition of solid surfaces and to determine their local chemical environment, specifically, the valence state (based on the specific binding energy measured for a particular type of photoelectron).<sup>71</sup> Therefore, XPS analysis was utilized to further determine the chemical species on the surface of the in-situ formed Co NPs in the PP matrix. The Co 2p XPS measurement of the 20.0 wt % Co NPs/PP/PP-g-MA MPNCs

was carried out to obtain the Co oxidation state on the Co NPs. As shown in Figure 4a, the binding energy peak of Co 2p<sub>3/2</sub> and

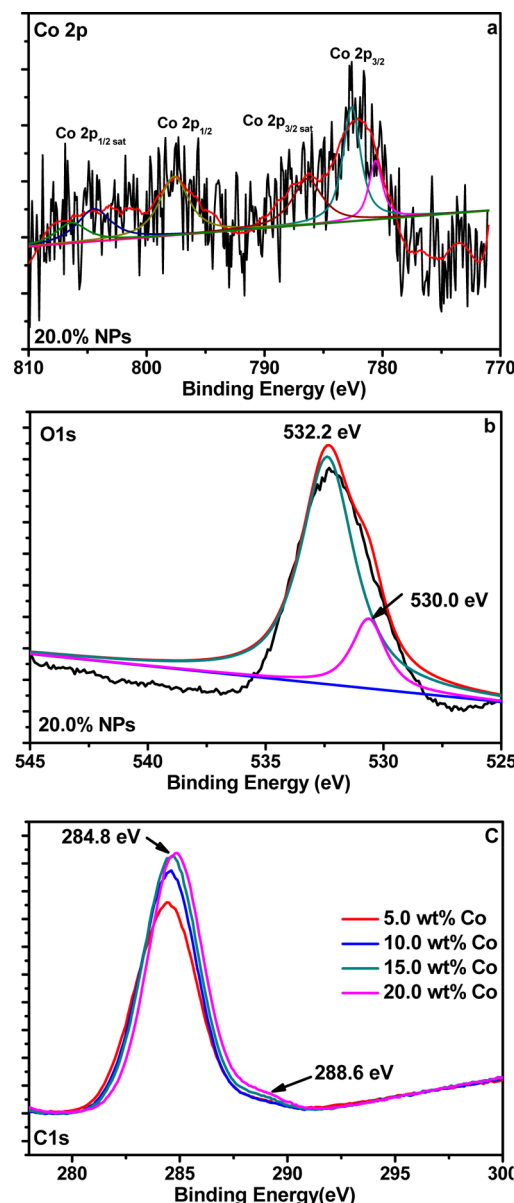


**Figure 4.** (a) Co 2p, (b) O 1s, and (c) C 1s XPS spectra of the PP/PP-g-MA/Co nanocomposites.

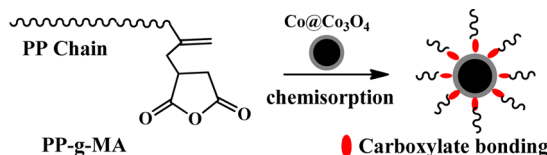
Co 2p<sub>1/2</sub> is located at ~780 eV (magenta and dark cyan curve) and 796 eV (dark yellow curve), respectively.<sup>72</sup> After the peak deconvolution, the peak of Co<sup>3+</sup> 2p<sub>3/2</sub> can be found at ~780.0 eV (magenta) and that of Co<sup>2+</sup> 2p<sub>3/2</sub> at ~782.0 eV (dark cyan), which are in good agreement with the reported Co<sub>3</sub>O<sub>4</sub>.<sup>73</sup> In addition, weak satellites located at ~787 eV (wine color curve) and 805 eV (olive color curve) can be observed in the Co 2p XPS spectra, which can also be assigned to Co<sub>3</sub>O<sub>4</sub>.<sup>72,74</sup> Despite the noisy background of the Co 2p XPS spectrum, it can be concluded that the majority of the Co atoms on the Co nanoparticle surface are Co<sub>3</sub>O<sub>4</sub>, indicating that the in-situ synthesized Co NPs are fully passivated by an oxide layer.

The O 1s spectrum (Figure 4b) depicts only one single O 1s peak at around 532.0 eV. Upon peak deconvolution, one binding energy peak is observed at ~532.2 eV (dark cyan),

which can be assigned to the carboxylate group,<sup>75</sup> and the peak at 530.0 eV (magenta) is consistent with the reported  $\text{Co}_3\text{O}_4$  O 1s spectrum.<sup>73,76</sup> Usually, the O 1s peak of PP-g-MA can be deconvoluted into two component peaks: the peak at 532.7 eV arises from the carbonyl oxygen ( $\text{C}=\text{O}$ ) of the maleic anhydride, whereas the peak at 533.8 eV arises from the ether oxygen ( $\text{C}-\text{O}-\text{C}$ ).<sup>77</sup> However, the symmetric peak at binding energy of  $\sim$ 532.2 eV further suggests the presence of two symmetric oxygen atoms in the carboxylate ( $\text{COO}^-$ ) group and the absence of the carbonyl ( $\text{C}=\text{O}$  bond) on the surface of Co NPs.<sup>75</sup> It indicates that the maleic anhydride in PP-g-MA has been hydrolyzed into two carboxylic groups during the synthesis of PP MPNCs, which can be chemisorbed onto the  $\text{Co}_3\text{O}_4$  surface,<sup>15</sup> resulting in two identical oxygen species from each  $\text{COO}^-$  group on the  $\text{Co}_3\text{O}_4$  surface.<sup>78–80</sup>

The C 1s spectrum (Figure 4c) depicts two peaks with binding energies at around 284.8 and 288.6 eV. The peak around 284.8 eV corresponds to the carbon atoms in the aliphatic chain (here it corresponds to the PP alkyl backbone). The shoulder peak at 288.6 eV is typically related to the chemisorbed surface carboxylate carbon,<sup>75,81,82</sup> which is obviously derived from the maleic anhydride groups in PP-g-MA. It must be noted that neither of these two peaks can be assigned to a carboxylic carbon, indicating that there is no free carboxylic acid present on the surface of these synthesized Co NPs.<sup>83</sup> Thus, the XPS results indicated that the  $\text{Co}_3\text{O}_4$  layer on the surface of these in-situ formed Co NPs was bound with the maleic anhydrides to form a strong chemical bonding during the synthetic process. The interaction between  $\text{Co}@\text{Co}_3\text{O}_4$  NPs and PP-g-MA is proposed and depicted in Scheme 2.

**Scheme 2. Proposed Interaction between  $\text{Co}@\text{Co}_3\text{O}_4$  NPs and PP-g-MA**



**3.3. Thermogravimetric Analysis (TGA).** Figures 5a and 5b show the TGA curves of the PP matrix and its MPNCs under nitrogen and air atmospheric condition, respectively. The detailed thermal decomposition temperatures are shown in Tables 1 and 2. Here, the initial thermal decomposition

**Table 1. TGA Characteristics of the Measured Samples under Nitrogen Atmosphere**

composition	$T_{\text{ini}}$ (°C) $\text{N}_2$	$T_{\text{max}}$ (°C)	residue at 700 °C (%)
pure PP	421.0	475.7	0.0
PP-g-MA	341.0	450.7	0.0
PP/5 wt % PP-g-MA	417.2	477.2	0.0
5.0 wt % NPs	446.0	480.0	4.8
10.0 wt % NPs	433.8	484.0	8.9
15.0 wt % NPs	431.1	482.0	16.5
20.0 wt % NPs	439.4	488.6	21.0
20.0 wt % NPs (no PP-g-MA)	409.0	481.4	20.2

**Table 2. TGA Characteristics of the Measured Samples under Air Atmosphere**

composition	$T_{\text{ini}}$ (°C) air	$T_{\text{max}}$ (°C)	residue at 700 °C (%)
pure PP	266.5	327.8	0.0
PP/5 wt % PP-g-MA	258.6	342.0	0.4
5.0 wt % NPs	316.2	406.4	6.2
10.0 wt % NPs	330.3	419.4	13.0
15.0 wt % NPs	341.4	438.6	20.9
20.0 wt % NPs	344.7	440.0	26.1
20.0 wt % NPs (no PP-g-MA)	330.6	432.0	26.2

temperature ( $T_{\text{ini}}$ ) is defined as the temperature when the specimen is at the 5% weight loss, while  $T_{\text{max}}$  (obtained from the differential analysis of TGA curve, DTG) is defined as the temperature when the specimen is experiencing its maximum rate of weight loss. The whole thermal degradation of pure PP under a nitrogen atmosphere only has one stage: it starts to decompose at 421 °C, and  $T_{\text{max}}$  is 475.7 °C with the main degradation occurring between 400 and 500 °C (Table 1). Pure PP does not leave any char residue at 700 °C.<sup>58</sup> Pure PP-g-MA starts to decompose at 341 °C, which is 80 °C earlier than that of pure PP (421 °C) and  $T_{\text{max}}$  is 450.7 °C with the main degradation occurred between 300 and 470 °C (Table 1). Pure PP-g-MA does not leave any char residue at 700 °C. Similarly, the blend of PP/5 wt % PP-g-MA also exhibits a one-step thermal degradation under nitrogen with a  $T_{\text{ini}}$  of 417.2 °C and  $T_{\text{max}}$  of 477.2 °C. The  $T_{\text{ini}}$  of the PP matrix is decreased by 3.8 °C after the incorporation of 5.0 wt % PP-g-MA, which is apparently due to the lower  $T_{\text{ini}}$  (Table 1) of the low molecular

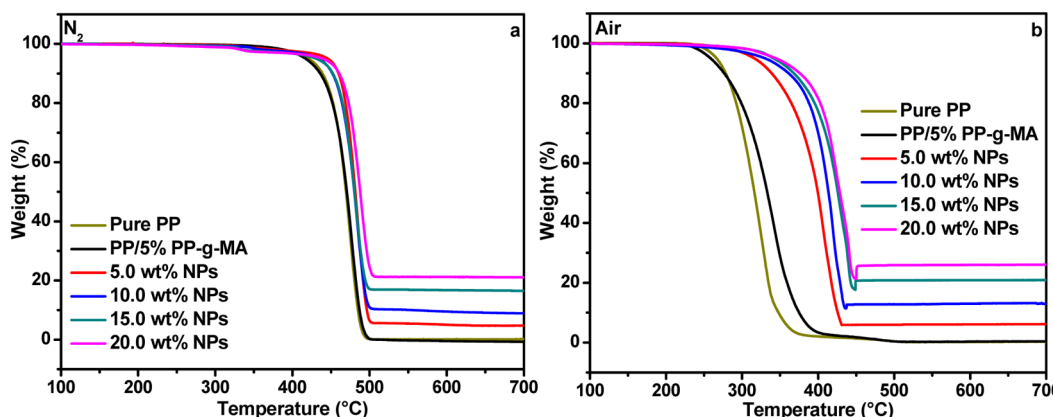
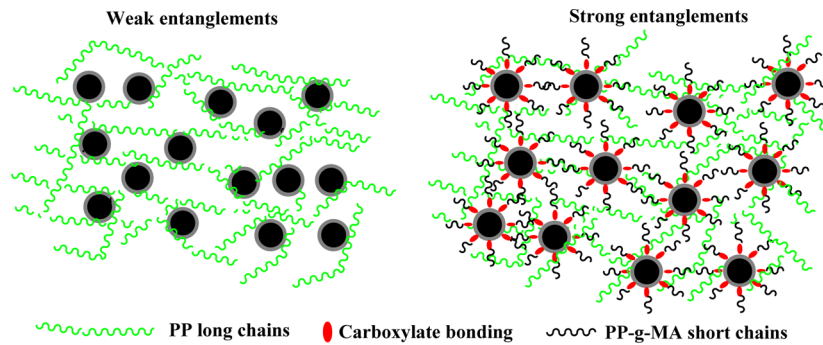


**Figure 5. TGA curves of pure PP and its nanocomposites under (a) nitrogen and (b) air atmosphere.**

**Scheme 3.** Proposed Mechanism of Interactions among PP, PP-g-MA, and Co NPs



weight PP-g-MA ( $M_n \approx 8000$ ) than that of the regular PP ( $M_n \approx 40\,500$ ). However, the strong entanglement between PP and PP-g-MA chains can reversely result in a slight increase of  $T_{max}$ . The PP/5 wt % PP-g-MA does not leave any char residue at 700 °C either. The thermal stability of the PP matrix stays almost intact after the incorporation of 5 wt % PP-g-MA under nitrogen.

After the incorporation of different loadings of NPs, both  $T_{\text{ini}}$  and  $T_{\text{max}}$  of these MPNCs are increased correspondingly (Figure 5a and Table 1). All the MPNCs exhibit mainly one-step degradation under nitrogen. With 5.0 wt % particle loading,  $T_{\text{ini}}$  increased significantly from 417.2 to 446.0 °C and  $T_{\text{max}}$  increased slightly from 477.2 to 480.0 °C. With further increase of the particle loading,  $T_{\text{ini}}$  decreased slightly but still higher than that of the pure PP matrix; meanwhile,  $T_{\text{max}}$  increased further to 488.6 °C when the particle loading reached 20.0 wt % (Table 1). The final residues at 700 °C are 4.8, 8.9, 16.5, and 21.0% in these MPNCs with a particle loading of 5.0, 10.0, 15.0, and 20.0 wt %, respectively. It can be concluded that the thermal stability of the PP matrix was enhanced by the in-situ synthesized Co NPs in the presence of PP-g-MA with the evidence of increased  $T_{\text{ini}}$  and  $T_{\text{max}}$  and high temperature residues.

With further investigation on the TGA of PP/20.0 wt % Co MPNCs, the role of PP-g-MA on the enhanced thermal stability of these PP MPNCs can be disclosed. For MPNCs with 20.0 wt % NPs, the  $T_{\text{ini}}$  decreased to 409.0 °C, which was 12 °C lower than that of pure PP (Table 1). Moreover, the  $T_{\text{ini}}$  is 30.4 °C lower than that of the MPNCs with 20.0 wt % Co NPs in the presence of PP-g-MA (439.4 °C). This indicates that in the absence of PP-g-MA, the incorporation of only Co NPs deteriorates the thermal stability of the PP matrix. Meanwhile, the  $T_{\text{max}}$  increased to 481.4 °C, which was only 5.7 °C higher than that of pure PP and was 7.2 °C lower than its counterpart with the presence of 5.0 wt % PP-g-MA. The final residue at 700 °C is 20.2%, which is 0.8% lower than that of the PP/5.0% PP-g-MA/20.0% Co MPNCs. All these observations indicated that the enhanced thermal stability of PP under nitrogen is primarily attributed to the strong interaction between PP-g-MA and Co NPs. As indicated from the above XPS analysis, the formed chemical bonding between the surface of Co NPs and the carboxylic groups from the hydrolysis of PP-g-MA can only be decomposed upon absorbing more energy during the temperature ramping in the thermal degradation of these PP MPNCs, and thus both increased  $T_{\text{ini}}$  and  $T_{\text{max}}$  are observed. Therefore, the entanglements between PP and PP-g-MA, and the strong chemical interactions between PP-g-MA and Co NPs, are primarily responsible for the enhanced thermal stability of PP matrix under nitrogen. In addition, with the aid

of 5.0% PP-g-MA, other probable reasons including the better dispersion quality of Co NPs in PP matrix as well as the reaction between the PP-g-MA bound Co NPs and the decomposition volatile products of PP can be also taken into account to further hinder the decomposition and yield higher thermal stability of the resulted PP/Co MPNCs than that of the PP/Co counterpart without PP-g-MA. The proposed mechanisms of the different interactions among PP, PP-g-MA, and the in-situ synthesized  $\text{Co}@\text{Co}_3\text{O}_4$  NPs are depicted in Scheme 3.

TGA measurements under air atmosphere were further investigated to determine the influences of the Co NPs on the thermal oxidative degradation of the PP matrix. Pure PP starts to decompose at 266.5 °C, and  $T_{\max}$  is 327.8 °C (Table 2). Meanwhile, pure PP does not leave any char residue at 700 °C under air. The PP/5.0 wt % PP-g-MA begins to decompose at around 258.6 °C with a  $T_{\max}$  of 342.0 °C under air atmosphere (Figure 5b), which are 158.6 and 135.2 °C ahead of its decomposition under inert atmosphere. PP/5 wt % PP-g-MA leaves almost no char residue at 700 °C under air. The thermal oxidative degradation of these MPNCs experienced differently when incorporated with the Co NPs. First, with only 5.0 wt % Co NPs,  $T_{\text{ini}}$  increased significantly from 258.6 to 316.2 °C and  $T_{\max}$  increased from 342.0 to 406.4 °C (Table 2), which were 57.6 and 64.4 °C higher than those of the PP/5 wt % PP-g-MA blend. Moreover,  $T_{\text{ini}}$  and  $T_{\max}$  were further increased to 344.7 and 440.0 °C when the particle loading was increased from 5.0 to 20.0 wt % (Table 2), which were 86.1 and 98.0 °C higher than those of the PP/5 wt % PP-g-MA blend. The oxidative residues at 700 °C are 6.2, 13.0, 20.9, and 26.1% for the PNCs with 5.0, 10.0, 15.0, and 20.0 wt % particle loadings. Apparently, the Co NPs effectively deferred the PP matrix from oxidative decomposition, indicating that the thermal oxidative stability of the MPNCs was significantly enhanced in the presence of the in-situ synthesized Co NPs.

In order to investigate the effects of PP-g-MA on the thermal oxidative stability improvement of the PP matrix, the PP/20.0 wt % Co MPNCs in the absence of PP-g-MA had also been prepared for comparison.  $T_{\text{ini}}$  increased from 258.6 to 330.6 °C and  $T_{\text{max}}$  increased from 342.0 to 432.0 °C upon the incorporation of 20.0 wt % Co NPs, which clearly revealed an enhanced thermal oxidative stability for the PP/20.0 wt % Co MPNCs. Compared with the PP/5.0% PP-g-MA/20.0% Co MPNCs (Table 2),  $T_{\text{ini}}$  of the PP/20.0 wt % Co MPNCs was decreased from 344.7 to 330.6 °C and  $T_{\text{max}}$  was decreased from 440.0 to 432.0 °C due to the absence of PP-g-MA. Again, from XPS analysis, it is clear that the addition of PP-g-MA can stabilize these in-situ Co NPs by chemisorbing PP-g-MA on the surface of  $\text{Co}_3\text{O}_4$  layer. Thus, the enhanced thermal oxidative stability by PP-g-MA is obviously attributed to the enhanced

stability of Co NPs in PP matrix, which requires higher energy to decompose when the PP/PP-g-MA/Co MPNCs was exposed under air.

**3.4. MCC Heat Release Parameters.** MCC was further utilized to determine the flammability of PP and its MPNCs with different loading of Co NPs. Figure 6 depicts the HRR vs

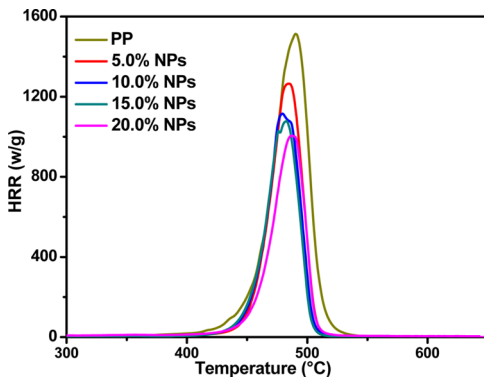


Figure 6. MCC curves of pure PP and its nanocomposites.

Table 3. MCC Data of the Measured Samples

composition	HRC (J/(g K))	PHRR (w/g)	T <sub>PHRR</sub> (°C)	THR (kJ/g)
pure PP	1187.0	1513.0	490.4	40.6
5.0 wt % NPs	1167.0	1262.0	484.6	39.0
10.0 wt % NPs	1047.0	1112.0	479.3	35.3
15.0 wt % NPs	1015.0	1027.0	476.2	33.7
20.0 wt % NPs	948.0	998.9	486.8	31.1

temperature curves, and Table 3 lists the corresponding heat release parameters. HRR is the most important parameter to assess the fire hazard of one flammable material.<sup>84</sup> PHRR is the maximum HRR which one material can generate the highest rate of heat release under explosion to certain fire scenario. In other words, the higher the PHRR is, the more dangerous one material will act under one specific fire accident.

PP is a highly flammable polymeric material (here with a PHRR of 1513 w/g), which limits its application in many engineering applications such as automotive industry. With the addition of Co NPs, PHRR, HRC, and THR of these MPNCs were observed to be decreased with increasing the Co particle loadings. To be specific, PHRR decreased from 1513.0 to 1262.0 w/g (~16.6% reduction) and to 998.9 w/g (~34.0% reduction), respectively, when 5.0 and 20.0% Co NPs were incorporated into the PP matrix. Moreover, the initial decomposition temperature was enhanced upon adding the Co NPs, which is consistent with TGA results under N<sub>2</sub>. Apparently, these in-situ synthesized Co NPs can act as flame retardant to reduce the flammability of the PP matrix. Because of the inert thermal decomposition approaches utilized to decompose all the samples before the combustible volatiles entering into the combustion chamber in this MCC measurement and the known enhanced thermal stability by Co NPs, the flame retardancy mechanism here is primarily attributed to a barrier effect formed from these Co NPs, which can slow down the heat and mass transfer between gas and condensed phases and prevent the polymeric material from fast decomposition when these MPNCs were exposed under heat.<sup>85</sup> Hence, the

reduced HRR indicated the lowered down combustible volatiles generated from these PP chains in the presence of Co NPs. Compared with the reported PP incorporated with 20.0 wt % traditional intumescence flame retardants (PHRR at 1171.0 w/g),<sup>69</sup> 20.0 wt % Co NPs resulted in ~14.7% lower in PHRR (998.9 w/g) for the PP matrix, which further suggests that the Co NPs can effectively reduce the flammability of the PP matrix through the high thermal stability shield effect. In addition, there is rare report on high loading metal@metal oxide core–shell NPs for flame retardant usage yet.

**3.5. Differential Scanning Calorimetry (DSC).** The DSC plots of the PP matrix and its MPNCs are presented in Figure 7, and the detailed data (melting peak temperature, T<sub>m</sub>;

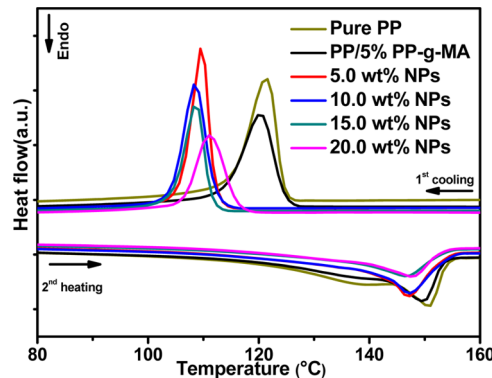


Figure 7. DSC curves of pure PP and its nanocomposites.

Table 4. DSC Characteristics of the Measured Samples

composition	T <sub>m</sub> (°C)	ΔH <sub>m</sub> (J/g)	T <sub>c</sub> (°C)	ΔH <sub>c</sub> (J/g)	F <sub>c</sub> (%)
pure PP	150.7	90.4	121.5	86.6	43.3
PP/5 wt % PP-g-MA	149.7	87.0	120.3	81.1	41.6
5.0 wt % NPs	148.1	80.8	110.6	81.0	40.7
10.0 wt % NPs	147.0	74.3	108.6	78.4	39.5
15.0 wt % NPs	146.7	61.6	108.6	64.2	34.7
20.0 wt % NPs	147.7	60.1	111.0	61.7	35.9

crystalline peak temperature, T<sub>c</sub>; heat of fusion, ΔH<sub>m</sub>; and crystalline fraction, F<sub>c</sub>) are summarized in Table 4. The crystalline fraction (F<sub>c</sub>) of the studied samples was determined according to eq 1:

$$F_c = \Delta H_m / [\Delta H_m^\circ (1 - x)] \quad (1)$$

where ΔH<sub>m</sub> is the measured heat of melting (direct integration of the melting peak area from DSC curves) and ΔH<sub>m</sub><sup>°</sup> is the heat of fusion of 100% crystal. Here, the theoretical value of ΔH<sub>m</sub><sup>°</sup> used is 209 J/g for PP,<sup>86,87</sup> and x is the loading of the NPs.

The PP/5.0 wt % PP-g-MA blend demonstrates a T<sub>m</sub> at 149.7 °C and T<sub>c</sub> at 120.3 °C, which are almost the same as those of pure PP (Table 4). However, the PP/5.0 wt % PP-g-MA blend has a F<sub>c</sub> of 41.6%, which is slightly lower than that of pure PP (43.3%). It is clear that F<sub>c</sub> is proportionate to ΔH<sub>m</sub> (eq 1); hence, the decrease in ΔH<sub>m</sub> directly results in a decreased F<sub>c</sub>, which is attributed to the lower ΔH<sub>m</sub> of this low molecular weight PP-g-MA.

Compared with the PP matrix, all these MPNCs show a slightly decreased T<sub>m</sub> and a significantly decreased T<sub>c</sub> (Figure 7) (detailed data are listed in Table 4). Actually, at high filler concentration, nanofillers like magnetic NPs can act as

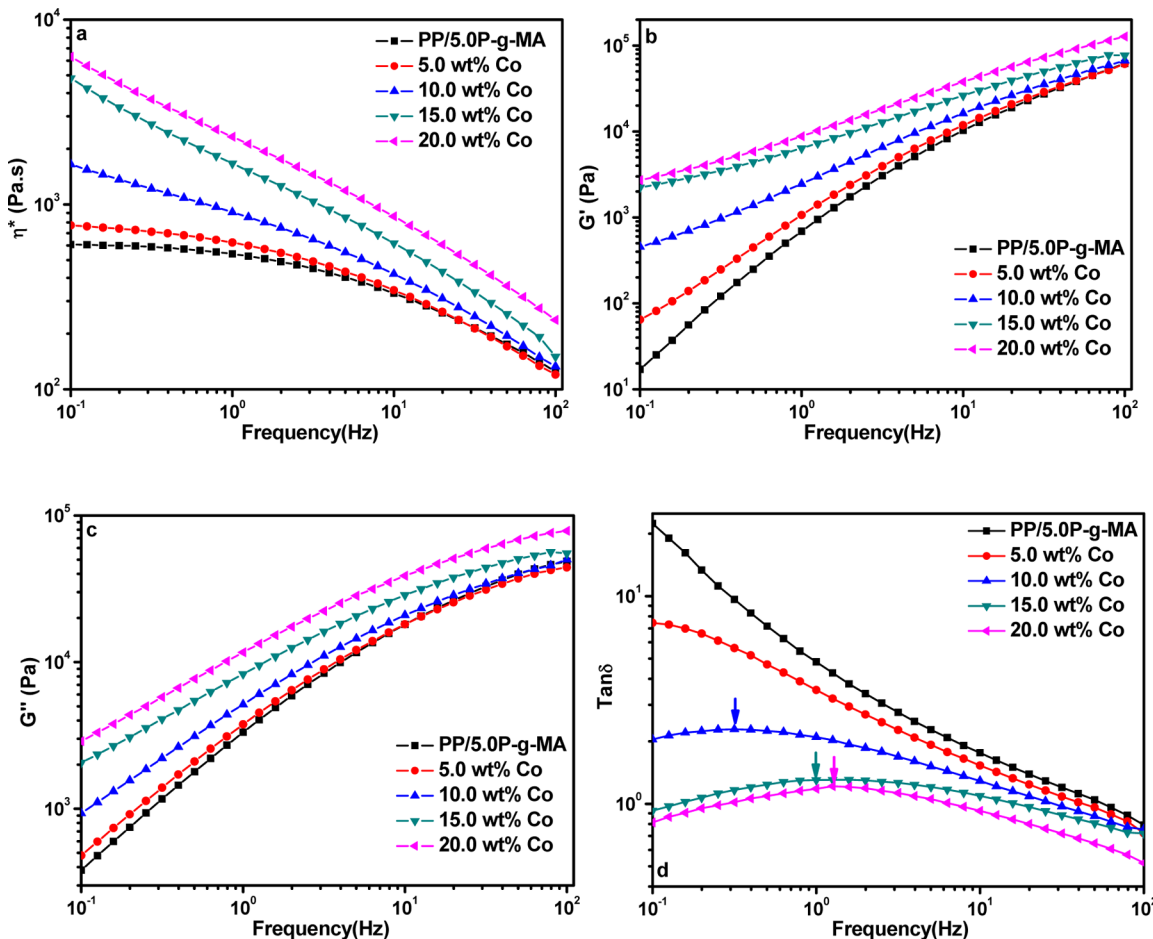


**Figure 8.** Melt rheological properties: (a) complex viscosity, (b) storage modulus, (c) loss modulus, and (d) damping property of PP and its nanocomposites with different particle loadings.

noncrystallizable barriers to disturb the crystal growth of polymer crystallization, which decreases the crystalline peak temperature by inversely decelerating the crystallization. Furthermore, the fillers may also hinder the mobility of the polymer chains, which in turn restricts the growth crystallites at a high filler concentration. However, when a critical loading is reached, such as 20.0 wt %, some Co NPs can serve as additional nucleation sites for crystallization and thus increase the crystallization rate of the hosting polymer. This effect is very limited as indicated by the slightly increased crystalline peak temperature. Meanwhile, significant decreases in  $\Delta H_m$  and  $\Delta H_c$  are observed. With 5.0 wt % NPs, the  $\Delta H_m$  of the MPNCs decreases significantly from 87.0 to 80.8 J/g. When the particle loading was further increased to 20.0 wt %, the  $\Delta H_m$  and  $\Delta H_c$  decreased to 60.1 and 61.7 J/g, respectively. The  $F_c$  is observed to decrease after the incorporation of the NPs ( $F_c$  decreased from 41.6 to 40.7% when PP/PP-g-MA matrix was incorporated with 5.0 wt % Co NPs and then decreased to 35.9% when the particle loading was further increased to 20.0 wt % NPs (Table 4)). This suggests that the crystallization of PP was partially suppressed, as the Co NPs can act as defects and thus introduce more grain boundaries, which effectively hinders the crystallization of PP segments.<sup>62</sup>

**3.6. Melt Rheological Behaviors.** The dispersion of the nanofillers in a polymer matrix has a significant impact on the rheological behaviors and thus influences the subsequent processing of these nanocomposite materials.<sup>88</sup> The differences

in rheological behaviors can in turn provide insights into the structural variations of the NPs dispersed in the hosting PP matrix. Figure 8a–d shows the frequency sweep curves of the complex viscosity ( $\eta^*$ ), storage modulus ( $G'$ ), loss modulus ( $G''$ ), and damping property ( $\tan \delta$ ) of the PP MPNC melts at 200 °C, respectively. Obviously, these in-situ synthesized NPs have a dramatic effect on the rheological behaviors of the MPNC melts. Figure 8a shows the  $\eta^*$  vs oscillation frequency curves of the PP matrix and its MPNCs with different nanoparticle loadings. The PP/PP-g-MA matrix exhibited frequency-independent fluid properties, i.e., Newtonian-type flow behavior at low oscillation frequency region (lower than 1.0 Hz), and further demonstrated a shear thinning ( $\eta^*$  decreases with an increase of oscillation frequency) behavior<sup>89,90</sup> thereafter until 100 Hz. Pure PP exhibited almost the same  $\eta^*$  as the PP/5.0% PP-g-MA blend within the whole frequency. For the MPNCs reinforced with 5.0 wt % NPs, the resulting  $\eta^*$  is similar to that of PP/PP-g-MA matrix within the frequency range between 0.1 and 100.0 Hz. One can be observed that the  $\eta^*$  is slightly higher than that of the PP/PP-g-MA matrix at the frequency range from 0.1 to 10.0 Hz. The similarity in  $\eta^*$  at high frequency (10.0–100.0 Hz) indicates a polymer melt rather than filler dominated fluid dynamics when only 5.0 wt % NPs were incorporated into the PP matrix.<sup>12</sup> When the particle loadings were further increased to 10.0 wt % and higher,  $\eta^*$  was increased sharply at the low-frequency region, and the  $\eta^*$  of PP/20.0 wt % NPs was about 2 orders of

magnitude higher than that of the PP matrix at 0.1 Hz (Figure 8a). Meanwhile, the  $\eta^*$  decreased monotonically within the whole oscillation frequency, indicating a typical shear thinning behavior of all these MPNCs (except the PP/5.0 wt % NPs specimen).

PP chains can be totally relaxed upon melt, but the chain relaxation and relative motion were slightly inhibited after the incorporation of low nanoparticle loading, i.e., 5.0 wt % Co NPs. Thus, the  $\eta^*$  slightly increased in the low-frequency range. However, the inhibition of the PP chains with such low concentration of NPs has little impact on  $\eta^*$  in the high-frequency range, such as 10.0 Hz and higher. From TEM observations in Figure 2a, it is clear that there is no particle interconnected structure formed in the PP matrix, which evidently proved that the separated Co NPs distributed in the PP matrix cannot impede the movement of PP main chains during the melting. When the particle loading was further increased to 10.0 wt % and even higher, the PP chain relaxation and relative movement were significantly restrained by the presence of high concentration of NPs, and all the MPNCs became "stiffer" when heated to melt. Hence, the resulting  $\eta^*$  curve became linear within the whole frequency range, suggesting a filler dominated fluid when these MPNCs had been melted.<sup>12</sup> The transition in  $\eta^*$  indicates that these MPNCs have reached a rheological percolation, at which the NPs form an interconnected network structure and effectively impede the motion of the PP main chains. This shows a strong agreement with the microstructures of the Co NPs depicted in the TEM graphs (Figure 2).

Figure 8b,c shows the  $G'$  and  $G''$  curves as a function of oscillation frequency. Upon melting at 200 °C, the PP chains were fully relaxed in the absence of any NPs and demonstrated a typical homogeneous polymer-like terminal behavior.  $G'$  and  $G''$  increase monotonically with increasing the particle loading in all the frequency range (Figure 8b,c). It can be seen from Figure 8b that  $G'$  was widely separated in the low-frequency range while it was only slightly separated in the high-frequency range when the particle loading was increased from 0 to 20.0 wt %. This phenomenon suggests the increased solidlike properties of the polymeric matrix if the oscillation frequency is low enough for the NPs to restrict the mobility of the polymer chains.<sup>91</sup> Similar observations were also reported in the HDPE/silicate<sup>91</sup> and HDPE/clay PNCs.<sup>92</sup> In addition, a percolation plateau was observed at low-frequency range (0.1–1.0 Hz) when the particle loading was higher than 5.0 wt % (Figure 8b). The  $G''$  was also observed linearly increased upon incorporation of the NPs in the PP matrix and further increased with increasing the particle loading, indicating an obvious energy dissipation effect of these in-situ synthesized NPs. From the previously reported literatures, this kind of "plateau" is due to either an interconnected structure of the NPs or a strong particle–polymer interaction.<sup>12,93</sup> According to the observation from TEM images when the particle loading exceeded 5.0 wt % (Figure 2c–f) and the SEM image (Figure 3), the formation of stabilized interconnected network Co nanostructure in the PP matrix is responsible for the percolation plateau. Meanwhile, as indicated by XPS and enhanced thermal stability from TGA result, the strong particle–polymer interactions through the stabilization effect of PP-g-MA also contribute to the percolation plateau.

The damping properties of these MPNCs were depicted through  $\tan \delta$  (the ratio of  $G''$  to  $G'$ ) as a function of oscillation frequency curves (Figure 8d). The  $\tan \delta$  of the PP/PP-g-MA

matrix decreased monotonously in the whole frequency range (0.1–100.0 Hz), while a significant decrease in  $\tan \delta$  was observed in all the MPNCs. Moreover, a broad peak was observed in all the MPNCs except in the PP/5.0 wt % NPs sample. The higher value in  $\tan \delta$  of pure PP than that of the MPNCs is due to the total relaxation of the PP chains at 200 °C, which makes the PP chain–chain movement more difficult and more interchain friction heat is generated during the oscillation. After the incorporation of the NPs, the polymer chain relaxation and the relative motion have been significantly restrained. Hence, the internal chain–chain friction heat produced was decreased when applying the same oscillation frequency. In addition, a lower  $\tan \delta$  value was observed upon further increasing the particle loading. This observation suggests a strong interaction between the NPs and the polymer matrix, which shows great agreement with the aforementioned TGA results. Both the energy dissipation and the relaxation of PP chains are increasingly impeded as the particle loading increases. For the MPNCs except PP/5.0 wt % NPs sample, a broad peak appears on each  $\tan \delta$  curve, and the peak shifts to a higher frequency with increasing particle loading due to the greater restrictions.<sup>12</sup> In the low-frequency range, the polymer chain motion keeps in step with the oscillation and the internal friction among the polymer chains would be negligible. Once the frequency further increases to the high range, the movement of the polymer chains is not able to catch up with the oscillation passing through the high-frequency range, resulting in a glass-state-like behavior<sup>12,50</sup> of these MPNCs and generating a small amount of energy loss. A large amount of energy loss appears between these two extreme conditions when the polymer shows viscoelastic properties.<sup>94</sup>

**3.7. Magnetic Property.** Figure 9 shows the room temperature magnetic hysteresis loops of the MPNCs with

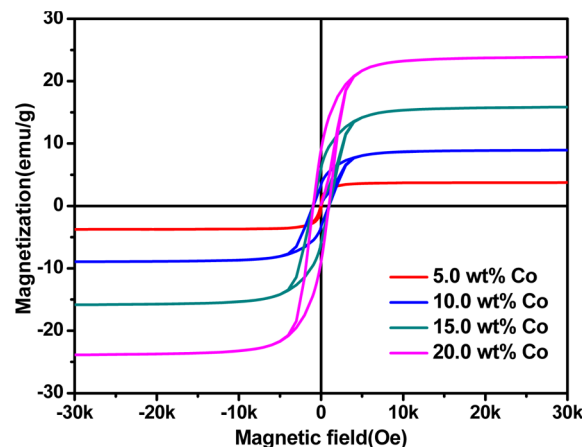


Figure 9. Room temperature magnetic hysteresis loops of the PP/PP-g-MA/Co nanocomposites with different particle loadings.

different particle loadings, and the detailed magnetic parameters are listed in Table 5. The saturation magnetization ( $M_s$ ) is

Table 5. Magnetic Properties of the Measured Samples

samples	$M_s$ (emu/g)	$M_s$ (emu/g Co)	$M_r$ (emu/g)	$H_c$ (Oe)
5.0 wt % NPs	3.8	76.0	0.43	47.0
10.0 wt % NPs	9.1	91.0	3.37	963.0
15.0 wt % NPs	16.1	107.3	5.95	990.0
20.0 wt % NPs	24.2	121.0	8.90	952.0

defined as the magnetization of one material which cannot be further increased with an increase of the external magnetic field. The  $M_s$  of all the MPNC samples tested is saturated at an external magnetic field of 30 kOe. Coercivity (coercive force,  $H_c$ ) is defined as the applied external magnetic field which is necessary to return one material to a zero magnetization condition.

For these MPNCs,  $M_s$  was increased significantly from 3.8 to 24.2 emu/(g composite) (Table 5) when the particle loading was increased from 5.0 to 20.0 wt %, which corresponds to 76.0, 91.0, 107.3, and 121.0 emu/(g Co). The bulk Co is ferromagnetic with a reported  $M_s$  of about 162 emu/g,<sup>26</sup> while the Co oxide is antiferromagnetic.<sup>95</sup> Apparently, the  $M_s$  of these as-prepared MPNCs is significantly lower than that of bulk Co. The reasons for these lower measured  $M_s$  are as follows: first, partial oxidation of the Co NPs, which in turn compromised the effective particle loading of the metallic Co in the MPNCs; second, loss of net magnetic moment due to the antiferromagnetic Co oxide shell on the top of metallic Co core.<sup>96</sup> The increased  $M_s$  with high Co loading indicated a decreased oxidation of these Co NPs. Moreover, when PP was reinforced with 20.0 wt % Co NPs without the stabilization of PP-g-MA, the  $M_s$  is only 19.5 emu/(g composite), which is 4.7 emu/g lower than its counterpart with PP-g-MA. Thus, it can be concluded that the stabilization of Co NPs by PP-g-MA also provides better passivation of these Co NPs with less oxidation. The  $H_c$  of the PP/5.0 wt % Co MPNCs is 47.0 Oe, indicating a soft ferromagnetic behavior. From Table 5, it is obvious that all the tested samples have a  $H_c$  significantly higher than 200 Oe (around 1000 Oe, Table 4) except the PP/5.0 wt % Co MPNCs, indicating a room temperature hard ferromagnetic behavior of these PP MPNCs. The significant difference in  $H_c$  can be referred to the intrinsic properties of the corresponding composites. When the PP MPNCs were reinforced with low particle loading, i.e., 5.0 wt %, the NPs were distributed in the PP matrix separately. With the assistance of PP-g-MA, the MAH functional groups tightly bound to the outer surface of the NPs; moreover, the resulting PP-g-MA main chains and PP chains further adsorbed onto the NPs. The repulsion forces from the introduced PP-g-MA and PP chains are stronger than the magnetic dipolar-dipolar forces and van der Waals forces, which led to the separated particles distributed in the PP matrix as confirmed from TEM in Figure 2a. The  $H_c$  of 47.0 Oe is comparable to the bulk value (a few tens Oe).<sup>95,97</sup> As the particle loading increased, the interparticle distances were decreased. The repulsion forces from the polymer chains are not strong enough to overcome the intrinsic magnetic dipolar-dipolar forces and thus cause the formation of Co nanowires due to the magnetic dipolar forces induced self-assembly effect.<sup>30,72,98</sup> The  $H_c$  of ~1000 Oe is probably due to (1) the formation of both Co nanowires and thin Co hexagonal plates, which can induce significant shape anisotropy, and (2) the exchange anisotropy/bias aroused between the ferromagnetic Co core and the antiferromagnetic Co oxide shell.<sup>26,99,100</sup> Here, despite the particle loading from 10.0 to 20.0 wt %,  $H_c$  is almost stable at ~1000 Oe. This indicated that the dominating effect of shape anisotropy controlled the high coercive forces because the dipolar interactions from stabilized cobalt wires prohibited the flipping of spins.<sup>99</sup> Such high coercive forces are favorable to fabricate magnetic storage devices.<sup>26</sup>

## 4. CONCLUSION

In summary, PP/Co MPNCs were successfully synthesized through a one-pot bottom-up wet chemistry method. The in-situ synthesized magnetic NPs consisting of metallic Co core covered by  $\text{Co}_3\text{O}_4$  shell were stabilized by PP-g-MA in the PP matrix. With different loadings, these Co NPs can result in different morphology and room temperature magnetic behaviors, such as individually dispersed NPs with soft ferromagnetic behavior and interconnected network structure with hard ferromagnetic behavior. In addition, the saturation magnetizations were enhanced by the formation of less oxide on the surface of Co NPs due to the stabilization of Co NPs by PP-g-MA. A rheological plateau was formed at low oscillation frequency due to both the strong particle–polymer interaction through PP-g-MA bridging and the formation of Co interconnected network structure in the hosting PP matrix with the particle loading between 5.0 and 10.0 wt %. Meanwhile, the thermal and oxidative stability of the thus-formed PP/PP-g-MA/Co MPNCs was enhanced, and the flammability of PP matrix was suppressed by adding these Co NPs. The merits of this method including large-scale and mild reaction conditions, in-situ route, and surfactant compatibility with many polymers and copolymers will facilitate the use of thermoplastic polymer-based MPNCs for potential applications such as magnetic information storage materials.

## ■ AUTHOR INFORMATION

### Corresponding Author

\*E-mail zhanhu.guo@lamar.edu, Ph (409) 880 7654 (Z.G.); e-mail suying.wei@lamar.edu, Ph (409) 880 7976 (S.W.).

### Notes

The authors declare no competing financial interest.

## ■ ACKNOWLEDGMENTS

This project is supported by the Seeded Research Enhancement Grant from Lamar University. Partial financial support from National Science Foundation–Chemical and Biological Separations (CBET: 11-37441) managed by Dr. Rosemarie D. Wesson is appreciated. We also appreciate the support from National Science Foundation Nanoscale Interdisciplinary Research Team and Materials Processing and Manufacturing (CMMI 10-30755) to purchase TGA and DSC. D. P. Young acknowledges support from the NSF under Grant DMR 10-05764.

## ■ REFERENCES

- (1) Kommareddi, N. S.; Tata, M.; John, V. T.; McPherson, G. L.; Herman, M. F.; Lee, Y. S.; O'Connor, C. J.; Akkara, J. A.; Kaplan, D. L. *Chem. Mater.* **1996**, *8*, 801–809.
- (2) Tang, B. Z.; Geng, Y.; Lam, J. W. Y.; Li, B.; Jing, X.; Wang, X.; Wang, F.; Pakhomov, A.; Zhang, X. *Chem. Mater.* **1999**, *11*, 1581–1589.
- (3) Tannenbaum, R.; Zubris, M.; Goldberg, E. P.; Reich, S.; Dan, N. *Macromolecules* **2005**, *38*, 4254–4259.
- (4) Guo, Z.; Henry, L. L.; Palshin, V.; Podlaha, E. J. *J. Mater. Chem.* **2006**, *16*, 1772–1777.
- (5) Guo, Z.; Park, S.; Hahn, H. T.; Wei, S.; Moldovan, M.; Karki, A. B.; Young, D. P. *Appl. Phys. Lett.* **2007**, *90*, 053111.
- (6) Guo, Z.; Lin, H.; Karki, A. B.; Wei, S.; Young, D. P.; Park, S.; Willis, J.; Hahn, T. H. *Compos. Sci. Technol.* **2008**, *68*, 2551–2556.
- (7) Guo, Z.; Lei, K.; Li, Y.; Ng, H. W.; Prikhodko, S.; Hahn, H. T. *Compos. Sci. Technol.* **2008**, *68*, 1513–1520.
- (8) Biswas, S.; Belfield, K. D.; Das, R. K.; Ghosh, S.; Hebard, A. F. *Chem. Mater.* **2009**, *21*, 5644–5653.

- (9) Zhu, J.; Wei, S.; Ryu, J.; Sun, L.; Luo, Z.; Guo, Z. *ACS Appl. Mater. Interfaces* **2010**, *2*, 2100–2107.
- (10) Hickey, R. J.; Haynes, A. S.; Kikkawa, J. M.; Park, S. J. *J. Am. Chem. Soc.* **2011**, *133*, 1517–1525.
- (11) Zhu, J.; Wei, S.; Li, Y.; Pallavkar, S.; Lin, H.; Haldolaarachchige, N.; Luo, Z.; Young, D. P.; Guo, Z. *J. Mater. Chem.* **2011**, *21*, 16239–16246.
- (12) Zhu, J.; Wei, S.; Li, Y.; Sun, L.; Haldolaarachchige, N.; Young, D. P.; Southworth, C.; Khasanov, A.; Luo, Z.; Guo, Z. *Macromolecules* **2011**, *44*, 4382–4391.
- (13) Wei, S.; Wang, Q.; Zhu, J.; Sun, L.; Lin, H.; Guo, Z. *Nanoscale* **2011**, *3*, 4474–4502.
- (14) Zhu, J.; Wei, S.; Lee, I. Y.; Park, S.; Willis, J.; Haldolaarachchige, N.; Young, D. P.; Luo, Z.; Guo, Z. *RSC Adv.* **2012**, *2*, 1136–1143.
- (15) He, Q.; Yuan, T.; Wei, S.; Haldolaarachchige, N.; Luo, Z.; Young, D. P.; Khasanov, A.; Guo, Z. *Angew. Chem., Int. Ed.* **2012**, *51*, 8842–8845.
- (16) Guo, Z.; Park, S.; Hahn, H. T.; Wei, S.; Moldovan, M.; Karki, A. B.; Young, D. P. *J. Appl. Phys.* **2007**, *101*, 09M511.
- (17) Goesmann, H.; Feldmann, C. *Angew. Chem., Int. Ed.* **2010**, *49*, 1362–1395.
- (18) Cheng, L.; Yang, K.; Li, Y.; Chen, J.; Wang, C.; Shao, M.; Lee, S.-T.; Liu, Z. *Angew. Chem., Int. Ed.* **2011**, *50*, 7385–7390.
- (19) Howes, P.; Green, M.; Bowers, A.; Parker, D.; Varma, G.; Kallumadil, M.; Hughes, M.; Warley, A.; Brain, A.; Botnar, R. *J. Am. Chem. Soc.* **2010**, *132*, 9833–9842.
- (20) Zhu, J.; Gu, H.; Rapole, S. B.; Luo, Z.; Pallavkar, S.; Haldolaarachchige, N.; Benson, T. J.; Ho, T. C.; Hopper, J.; Young, D. P.; Wei, S.; Guo, Z. *RSC Adv.* **2012**, *2*, 4844–4856.
- (21) Hoare, T.; Timko, B. P.; Santamaría, J.; Goya, G. F.; Irusta, S.; Lau, S.; Stefanescu, C. F.; Lin, D.; Langer, R.; Kohane, D. S. *Nano Lett.* **2011**, *11*, 1395–1400.
- (22) Zalich, M. A.; Baranauskas, V. V.; Riffle, J. S.; Saunders, M.; Pierre, T. G. S. *Chem. Mater.* **2006**, *18*, 2648–2655.
- (23) Zhang, X. H.; Ho, K. M.; Wu, A. H.; Wong, K. H.; Li, P. *Langmuir* **2010**, *26*, 6009–6014.
- (24) Puntes, V. F.; Krishnan, K. M.; Alivisatos, A. P. *Science* **2001**, *291*, 2115–2117.
- (25) Diana, F. S.; Lee, S. H.; Petroff, P. M.; Kramer, E. J. *Nano Lett.* **2003**, *3*, 891–895.
- (26) Srikala, D.; Singh, V.; Banerjee, A.; Mehta, B.; Patnaik, S. *J. Phys. Chem. C* **2008**, *112*, 13882–13885.
- (27) Tripp, S. L.; Pusztay, S. V.; Ribbe, A. E.; Wei, A. *J. Am. Chem. Soc.* **2002**, *124*, 7914–7915.
- (28) Zhou, Z.; Liu, G.; Han, D. *ACS Nano* **2009**, *3*, 165–172.
- (29) Baranauskas, V., III; Zalich, M.; Saunders, M.; Pierre, T. G. S.; Riffle, J. *Chem. Mater.* **2005**, *17*, 5246–5254.
- (30) Keng, P. Y.; Shim, I.; Korth, B. D.; Douglas, J. F.; Pyun, J. *ACS Nano* **2007**, *1*, 279–292.
- (31) Abes, J.; Cohen, R.; Ross, C. *Chem. Mater.* **2003**, *15*, 1125–1131.
- (32) Robinson, I.; Volk, M.; Tung, L. D.; Caruntu, G.; Kay, N.; Thanh, N. T. K. *J. Phys. Chem. C* **2009**, *113*, 9497–9501.
- (33) Zalich, M. A.; Vadala, M. L.; Riffle, J. S.; Saunders, M.; St. Pierre, T. G. *Chem. Mater.* **2007**, *19*, 6597–6604.
- (34) de Silva, R. M.; Palshin, V.; Fronczeck, F. R.; Hormes, J.; Kumar, C. S. S. R. *J. Phys. Chem. C* **2007**, *111*, 10320–10328.
- (35) Lagunas, A.; Jimeno, C.; Font, D.; Solà, L.; Pericàs, M. A. *Langmuir* **2006**, *22*, 3823–3829.
- (36) Bao, Y.; An, W.; Turner, C. H.; Krishnan, K. M. *Langmuir* **2010**, *26*, 478–483.
- (37) Cheng, G.; Romero, D.; Fraser, G. T.; Walker, A. R. H. *Langmuir* **2005**, *21*, 12055–12059.
- (38) Pohjalainen, E.; Pohjakallio, M.; Johans, C.; Kontturi, K.; Timonen, J. V. I.; Ikkala, O.; Ras, R. H. A.; Viitala, T.; Heino, M. T.; Seppälä, E. T. *Langmuir* **2010**, *26*, 13937–13943.
- (39) Cheng, G.; Dennis, C. L.; Shull, R. D.; Walker, A. R. H. *Langmuir* **2007**, *23*, 11740–11746.
- (40) Liu, G.; Yan, X.; Lu, Z.; Curda, S. A.; Lal, J. *Chem. Mater.* **2005**, *17*, 4985–4991.
- (41) Qiao, R.; Zhang, X. L.; Qiu, R.; Kim, J. C.; Kang, Y. S. *Chem. Mater.* **2007**, *19*, 6485–6491.
- (42) Miinea, L. A.; Laura, B.; Ericson, K. D.; Glueck, D. S.; Grubbs, R. B. *Macromolecules* **2004**, *37*, 8967–8972.
- (43) Guo, L.; Liang, F.; Wang, N.; Kong, D.; Wang, S.; He, L.; Chen, C.; Meng, X.; Wu, Z. *Chem. Mater.* **2008**, *20*, 5163–5168.
- (44) Zhao, N.; Liu, S. *Eur. Polym. J.* **2011**, *47*, 1654–1663.
- (45) Roes, A.; Marsili, E.; Nieuwlaar, E.; Patel, M. *J. Polym. Environ.* **2007**, *15*, 212–226.
- (46) Grigoriadou, I.; Paraskevopoulos, K.; Chrissafis, K.; Pavlidou, E.; Stamkopoulos, T. G.; Bikaris, D. *Polym. Degrad. Stab.* **2010**, *96*, 151–163.
- (47) Garcés, J. M.; Moll, D. J.; Bicerano, J.; Fibiger, R.; McLeod, D. G. *Adv. Mater.* **2000**, *12*, 1835–1839.
- (48) McAuley, J. W. *Environ. Sci. Technol.* **2003**, *37*, 5414–5416.
- (49) Lee, J.-I.; Yang, S.-B.; Jung, H.-T. *Macromolecules* **2009**, *42*, 8328–8334.
- (50) Chen, X.; Wei, S.; Yadav, A.; Patil, R.; Zhu, J.; Ximenes, R.; Sun, L.; Guo, Z. *Macromol. Mater. Eng.* **2011**, *296*, 434–443.
- (51) Li, Y.; Zhu, J.; Wei, S.; Ryu, J.; Sun, L.; Guo, Z. *Macromol. Chem. Phys.* **2011**, *212*, 1951–1959.
- (52) Wei, S.; Patil, R.; Sun, L.; Haldolaarachchige, N.; Chen, X.; Young, D. P.; Guo, Z. *Macromol. Mater. Eng.* **2011**, *296*, 850–857.
- (53) Wong, S.-C.; Lee, H.; Qu, S.; Mall, S.; Chen, L. *Polymer* **2006**, *47*, 7477–7484.
- (54) Perilla, J. E.; Lee, B.-J.; Jana, S. C. *J. Rheol.* **2010**, *54*, 761–779.
- (55) Dai, P.; Zhang, W.; Pan, Y.; Chen, J.; Wang, Y.; Yao, D. *Composites, Part B* **2011**, *42*, 1144–1150.
- (56) Tanniru, M.; Yuan, Q.; Misra, R. *Polymer* **2006**, *47*, 2133–2146.
- (57) Jeon, K.; Lumata, L.; Tokumoto, T.; Steven, E.; Brooks, J.; Alamo, R. G. *Polymer* **2007**, *48*, 4751–4764.
- (58) Chow, W.; Mohd Ishak, Z.; Karger-Kocsis, J.; Apostolov, A.; Ishiaku, U. *Polymer* **2003**, *44*, 7427–7440.
- (59) Vladimirov, V.; Betchev, C.; Vassiliou, A.; Papageorgiou, G.; Bikaris, D. *Compos. Sci. Technol.* **2006**, *66*, 2935–2944.
- (60) Morlat, S.; Mailhot, B.; Gonzalez, D.; Gardette, J. L. *Chem. Mater.* **2004**, *16*, 377–383.
- (61) Galgali, G.; Ramesh, C.; Lele, A. *Macromolecules* **2001**, *34*, 852–858.
- (62) Purohit, P. J.; Huacuja-Sánchez, J. E.; Wang, D. Y.; Emmerling, F.; Thünemann, A.; Heinrich, G.; Schönhals, A. *Macromolecules* **2011**, *44*, 4342–4354.
- (63) Yu, H.; Zhang, Z.; Wang, Z.; Jiang, Z.; Liu, J.; Wang, L.; Wan, D.; Tang, T. *J. Phys. Chem. C* **2010**, *114*, 13226–13233.
- (64) Hsiao, M. C.; Liao, S. H.; Lin, Y. F.; Weng, C. C.; Tsai, H. M.; Ma, C. C. M.; Lee, S. H.; Yen, M. Y.; Liu, P. I. *Energy Environ. Sci.* **2011**, *4*, 543–550.
- (65) Chiu, S. H.; Wang, W. K. *J. Appl. Polym. Sci.* **1998**, *67*, 989–995.
- (66) Chen, X.; Yu, J.; Guo, S.; Lu, S.; Luo, Z.; He, M. *J. Mater. Sci.* **2009**, *44*, 1324–1332.
- (67) Wu, K.; Song, L.; Wang, Z.; Hu, Y. *J. Polym. Res.* **2009**, *16*, 283–294.
- (68) He, Q.; Lu, H.; Song, L.; Hu, Y.; Chen, L. *J. Fire Sci.* **2009**, *27*, 303–321.
- (69) Zhang, P.; Song, L.; Lu, H.; Hu, Y.; Xing, W.; Ni, J.; Wang, J. *Polym. Degrad. Stab.* **2009**, *94*, 201–207.
- (70) Puntes, V. F.; Zanchet, D.; Erdonmez, C. K.; Alivisatos, A. P. *J. Am. Chem. Soc.* **2002**, *124*, 12874–12880.
- (71) Zaera, F. *Chem. Rev.* **2012**, *112*, 2920–2986.
- (72) Keng, P. Y.; Kim, B. Y.; Shim, I. B.; Sahoo, R.; Veneman, P. E.; Armstrong, N. R.; Yoo, H.; Pemberton, J. E.; Bull, M. M.; Griebel, J. J. *ACS Nano* **2009**, *3*, 3143–3157.
- (73) Zhu, J.; Kailasam, K.; Fischer, A.; Thomas, A. *ACS Catal.* **2011**, *1*, 342–347.
- (74) Khodakov, A. Y.; Chu, W.; Fongarland, P. *Chem. Rev.* **2007**, *107*, 1692–1744.

- (75) Wu, N.; Fu, L.; Su, M.; Aslam, M.; Wong, K. C.; Dravid, V. P. *Nano Lett.* **2004**, *4*, 383–386.
- (76) Natile, M. M.; Glisenti, A. *Chem. Mater.* **2003**, *15*, 2502–2510.
- (77) Yang, B. X.; Shi, J. H.; Pramoda, K.; Goh, S. H. *Compos. Sci. Technol.* **2008**, *68*, 2490–2497.
- (78) Ciprari, D.; Jacob, K.; Tannenbaum, R. *Macromolecules* **2006**, *39*, 6565–6573.
- (79) King, S.; Hyunh, K.; Tannenbaum, R. *J. Phys. Chem. B* **2003**, *107*, 12097–12104.
- (80) Tannenbaum, R.; Zubris, M.; David, K.; Ciprari, D.; Jacob, K.; Jasiuk, I.; Dan, N. *J. Phys. Chem. B* **2006**, *110*, 2227–2232.
- (81) Frydman, E.; Cohen, H.; Maoz, R.; Sagiv, J. *Langmuir* **1997**, *13*, 5089–5106.
- (82) De Palma, R.; Peeters, S.; Van Bael, M. J.; Van den Rul, H.; Bonroy, K.; Laureyn, W.; Mullens, J.; Borghs, G.; Maes, G. *Chem. Mater.* **2007**, *19*, 1821–1831.
- (83) Willis, A. L.; Turro, N. J.; O'Brien, S. *Chem. Mater.* **2005**, *17*, 5970–5975.
- (84) Babrauskas, V.; Peacock, R. D. *Fire Saf. J.* **1992**, *18*, 255–272.
- (85) Wang, X.; Song, L.; Yang, H.; Xing, W.; Lu, H.; Hu, Y. *J. Mater. Chem.* **2012**, *22*, 3426–3431.
- (86) Carlson, E. D.; Krejchi, M. T.; Shah, C. D.; Terakawa, T.; Waymouth, R. M.; Fuller, G. G. *Macromolecules* **1998**, *31*, 5343–5351.
- (87) Rozanski, A.; Galeski, A.; Debowska, M. *Macromolecules* **2011**, *44*, 20–28.
- (88) Xu, D. H.; Wang, Z. G.; Douglas, J. F. *Macromolecules* **2008**, *41*, 815–825.
- (89) Kim, J.; Hong, S. M.; Kwak, S.; Seo, Y. *Phys. Chem. Chem. Phys.* **2009**, *11*, 10851–10859.
- (90) Wood-Adams, P. M.; Dealy, J. M.; Willem deGroot, A.; Redwine, O. D. *Macromolecules* **2000**, *33*, 7489–7499.
- (91) Chae, D. W.; Kim, K. J.; Kim, B. C. *Polymer* **2006**, *47*, 3609–3615.
- (92) Swain, S. K.; Isayev, A. I. *Polymer* **2007**, *48*, 281–289.
- (93) Pötschke, P.; Abdel-Goad, M.; Alig, I.; Dudkin, S.; Lellinger, D. *Polymer* **2004**, *45*, 8863–8870.
- (94) Bower, D. I. *An Introduction to Polymer Physics*; Cambridge University Press: New York, 2002.
- (95) Gao, C.; Liang, Y.; Han, M.; Xu, Z.; Zhu, J. *J. Phys. Chem. C* **2008**, *112*, 9272–9277.
- (96) Leslie-Pelecky, D. L.; Rieke, R. D. *Chem. Mater.* **1996**, *8*, 1770–1783.
- (97) Xu, R.; Xie, T.; Zhao, Y.; Li, Y. *Cryst. Growth Des.* **2007**, *7*, 1904–1911.
- (98) Sudeep, P.; Emrick, T. *ACS Nano* **2009**, *3*, 2870–2875.
- (99) Jun, Y.; Choi, J.; Cheon, J. *Chem. Commun.* **2007**, *47*, 5001–5003.
- (100) Salabas, E. L.; Rumplecker, A.; Kleitz, F.; Radu, F.; Schüth, F. *Nano Lett.* **2006**, *6*, 2977–2981.